Johann Wolfgang Goethe Universität Frankfurt am Main
Institut für Kernphysik

Fachbereich Physik

Bachelorarbeit

im Studiengang Physik

Thema: XUV-IR femtosecond pump-probe experiments on O_2 fragmentation

eingereicht von: Florian Wilhelm ‹wilhelm-florian@stud.uni-frankfurt.de›

eingereicht am: 29. September 2014

Erstgutachter: Herr Prof. Dr. Reinhard Dörner

Zweitgutachter: PD Dr. Till Jahnke

We must be clear that when it comes to atoms, language can be used only as in poetry. The poet, too, is not nearly so concerned with describing facts as with creating images and establishing mental connections.

by Niels Bohr

Abstract

Modern lasers capable of producing intense femtosecond light pulses opened a way to study light-induced non-linear processes and to visualize in real time light-induced molecular reactions. In this thesis a combination of infrared (IR) laser pulses and their higher-order harmonics in the extreme-ultraviolet domain (XUV) was used to map photodissociation dynamics in oxygen molecules. In the experiments performed using the Kansas Light Source (wavelength 800 nm, photon energy 1.55 eV) at the J.R. Macdonald Laboratory its 11th harmonic (photon energy $\sim$ 17.3 eV, pulse duration $\sim$ 100 fs) ionized neutral O_2 molecules, launching a nuclear wave packet on O_2^+ potential curves slightly below its dissociating threshold. The created molecular ions were dissociated by a synchronized fundamental laser pulse arriving after a well-defined femtosecond time delay, and the produced O^+ fragments were characterized employing recoil-ion momentum spectroscopy. The experiment revealed two different dissociation pathways corresponding to the net absorption of one and two infrared photons. The two channels showed very different dependence on the XUV-IR delay, with the contribution of the two-photon mechanism becoming negligible in $\sim$ 200 femtosecond after the XUV pulse.

Contents

List of Figures

Acknowledgements

First of all I would like to thank Assistant Professor Artem Rudenko who was my supervisor during my stay at Kansas State University. He always had an ear for his students and gave us a hand whenever we faced some issues. Second I would like to thank Professor Reinhard Dörner. He was my supervisor in Frankfurt and set the communication to Artem Rudenko. Doing an internship at K-State and writing my bachelor thesis in Kansas was initially his idea. I thank Till Jahnke for being by second assessor.

Many thanks to Wei Cao - a former PhD Student at K-State. Daniel Trabert and I took over his set up. He taught us how to operate it during our first weeks in the lab although he was already due to leave for a postdoctoral research position at the Lawrence Berkeley National Laboratory. I also want to thank Yubaraj Malakar. He helped us with the signal processing and data analysis. He introduced SpecTcl to the set up for data recording and live analysis.

Special thanks go to the German Academic Exchange Service (DAAD). They made my whole internship at K-State possible by supporting me financially and setting my insurances.

I am also thanking all my classmates for all those stimulating and informative discussions and for all the support during my studies.

1 Introduction

Over time the comprehension of atoms and molecules changed dramatically. Around 500 BC Greek philosophers like Leukipp and Demokrit thought of elementary indivisible particles, which they called "atoms". This idea was accepted roughly 2000 years later by Robert Boyle in his book "The Sceptical Chymist" (1661) and by Isaac Newton in "Principia" (1687) as well as in "Opticks" (1704) [6, 7]. It took many years to realise, that these atoms are not elementary and composed of other particles, namely electrons, protons and neutrons. They behave in a very non-intuitive way and can be described by probabilities and wave-equations. This rather new understanding of microscopic objects ended up in quantum mechanics. To unravel the nature of quantum worlds many experiments had been done, but there is still much more to discover. One of those exciting fields is time resolved molecular dynamics. Atomic motion in molecular reactions typically occurs on a femtosecond time scale. Therefore a high temporal resolution is needed for probing these processes. This work aimed at mapping photodissociation of simple molecules by a combination of infrared (IR) laser pulses and their higher-order harmonics. All experiments in this thesis had been done during a research internship at the James R. Macdonald laboratory of Kansas State University. We used an XUV-IR femtosecond pump-probe set up, which was built by Wei Cao. He taught us how to operate the set up and the laser on our own. In our pump-probe experiments the state of interest is reached by an extreme ultraviolet (XUV) laser pulse. Then an infrared (IR) laser pulse is used to probe the molecule. The charged fragments are detected using recoil-ion and electron momentum spectrometer. By recording the time of flight (TOF) and by using a position sensitive detector (PSD) the momenta and therefore the trajectories and energies of all fragments can be reconstructed. During our research internship at K-State Daniel Trabert and I did XUV-IR pump-probe experiments on neon, molecular oxygen, molecular deuterium and carbon dioxide. This thesis is mainly concentrating on O_2 fragmentation. Daniels bachelor thesis is going to treat D_2 and CO_2 fragmentations. For O_2 we were interested in an energy region that can be populated with the 11th harmonic of a 800 nm laser. This region lays between 17.0 and 17.5 eV and can populate the $O_2^+ a^4\Pi_u$ and $O_2^+ \tilde{A}^2\Pi_u$ state. Then the molecule is dissociated by the IR-probe pulse, most likely via $f^4\Pi_g$ repulsive state. The delay dependence of the measured oxygen ion yields and their kinetic energies on the XUV-pump and IR-probe can give us information about the dynamics of dissociation. The specific feature of these experiments compared to the other pump-probe studies employing higher order harmonics is a possibility to select a narrow bandwidth for the XUV pulse using a double-grating monochromator. This results in a possibility to populate one particular state of interest, even though the pump pulse becomes rather long ($\sim$ 100 fs). This state selective configuration provides information complementary to the experiments using ultrafast (few femtoseconds)

broadband harmonic pulses. This thesis is organized as follows: in Chapter 2 theoretical background for the performed studies is presented, followed by a description of the experimental set up in Chapter 3. The performed experiments are explained and discussed in Chapter 4. Finally a short summary, conclusions and outlooks are given in Chapter 5.

2 Theoretical background

2.1 Electromagnetic waves

> "When a charge undergoes *acceleration*, a portion of the field 'detaches' itself, in a sense, and travels off at the speed of light, carrying with it energy, momentum, and angular momentum. We call this **electromagnetic radiation**."
>
> by David J. Griffiths [8, p. xiv]

From electrodynamics one knows the importance of the Maxwell equations, which in vacuum read as follows [8]:

$$\nabla\vec{E} = 0 \qquad \nabla \times \vec{E} = -\frac{\partial\vec{B}}{\partial t} \tag{2.1}$$

$$\nabla\vec{B} = 0 \qquad \nabla \times \vec{B} = \mu_0\epsilon_0\frac{\partial\vec{E}}{\partial t} \tag{2.2}$$

The decoupled equations fulfil the wave equation for $f = \vec{B}$ and $f = \vec{E}$:

$$\nabla^2 f = \frac{1}{v^2}\frac{\partial^2 f}{\partial t^2} \tag{2.3}$$

Thus electromagnetic waves travel at the speed $v = \frac{1}{\sqrt{\mu_0\epsilon_0}} = c$. Assuming plane waves propagating in z-direction, the solution for equation 2.3 can be written in the form:

$$\tilde{\vec{E}} = \tilde{\vec{E}}_0 e^{i(kz-\omega t)} \tag{2.4}$$

$$\tilde{\vec{B}} = \tilde{\vec{B}}_0 e^{i(kz-\omega t)} \tag{2.5}$$

where the real parts represent the physical quantities of $\vec{E}$ and $\vec{B}$. Because $\nabla\vec{E} = 0$ and $\nabla\vec{B} = 0$ it must be true that $\tilde{E}_{0_z} = \tilde{B}_{0_z} = 0$. This means that electromagnetic waves are transverse and due to Faraday's law that $\vec{E}$ and $\vec{B}$ are perpendicular [8].

Polarization

The polarization is by convention given by the electrical Field $\vec{E}$. All kinds of polarization can be obtained by a superposition of two plane waves:

$$\tilde{\vec{E}}(\vec{r},t) = \tilde{E}_1 e^{i(k\vec{r}-\omega t)}\vec{n}_1 + \tilde{E}_2 e^{i(k\vec{r}-\omega t)}\vec{n}_2 \tag{2.6}$$

$\vec{n}_1$ and $\vec{n}_2$ are the polarization vectors of the two waves. To allow different phases between the waves, $\tilde{E}_1$ and $\tilde{E}_2$ are complex numbers. If both waves are in phase,

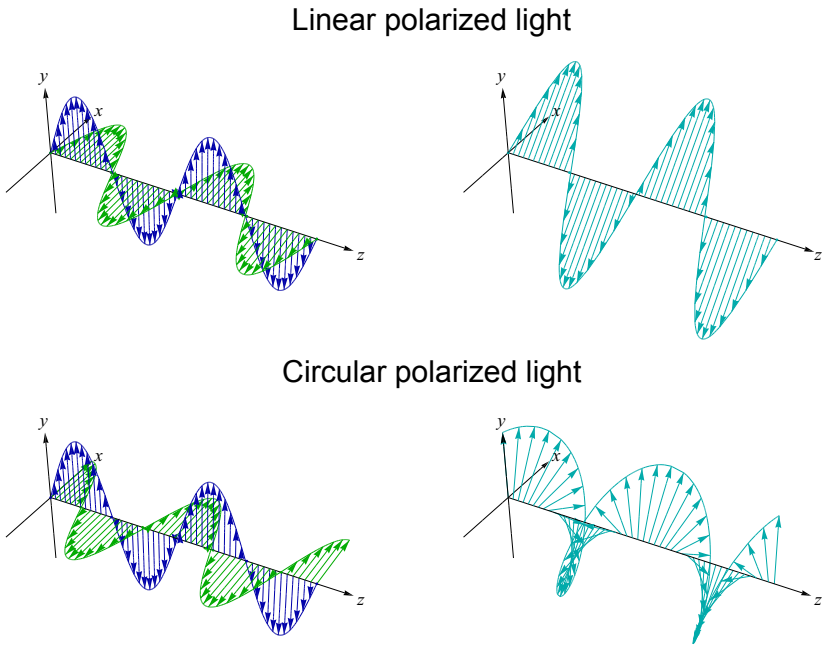

Figure 2.1: Linear and circular polarized light (own illustration)
Propagation in z-direction, $\vec{E}=\vec{E_1}+\vec{E_2}$

the polarization is linear (as shown as in the upper part of figure 2.1). A phase-difference other than zero leads to an elliptical polarization. A special case of this is circular polarized light, at which the amplitudes of $\tilde{E}_1$ and $\tilde{E}_2$ are equal but the phase-difference is $\frac{1}{2}\pi$ (illustrated in the lower part of figure 2.1) [9].

2.2 Photo-ionization

The common approach to describe the photoelectric effect was set by Albert Einstein. He introduced the quantization of light. In this "Einstein picture" an atom can only be photo-ionized by photons which have at least the energy of the ionization potential. Hereafter this process is referred as "single photon ionization". This way the kinetic energy of the photo electron is independent of the photon intensity. $E_{e_{ph}}$ is specified only by the frequency ν of the photon [7]:

$$E_{e_{ph}} = h\nu - I_p \tag{2.7}$$

Here I_p refers to the ionization energy.

Multi photon ionization

In modern physics we are not limited to single photon ionization. In intense laser fields it is possible to absorb multiple photons simultaneously. The N-photon ionization rate depends on the laser intensity and is given by [10]:

$$r_{_N} = \sigma_{_N} I^N \tag{2.8}$$

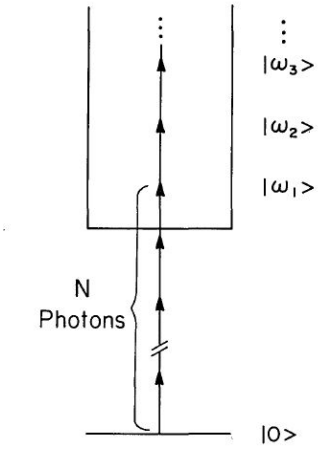

Figure 2.2: Energy scheme for above-threshold ionization (from [1])

σ_N denotes the N-photon ionization rate. After absorbing N photons the photoelectron energy reads as follows:

$$E_{e_{ph}} = N \cdot h\nu - I_p \tag{2.9}$$

The response of atoms in intense laser fields is highly non-linear and cannot be described by a perturbative theory [10].

Above-Threshold Ionization (ATI)

Due to the fact that a free electron cannot absorb photons, one could conclude that N in equation 2.9 refers to the minimum amount of photons required to reach the ionization threshold [10]. However, because of the presence of the parent ion there is a way to absorb even more photons. The process is illustrated in figure 2.2. $|0\rangle$ is the ground state. After absorbing N photons the $|\omega_1\rangle$-state is reached which is above the ionization potential. The states $|\omega_2\rangle$, $|\omega_3\rangle$ and so on are populated if one, two or more additional photons are absorbed [1]. This is only possible while the electron sits in the field of its parent ion, which is necessary for momentum conservation. The ion acts like a momentum reservoir [10].

2.3 High Harmonics Generation

High-harmonic generation (HHG) is a non-linear multi photon process. A driving laser field forces atoms or molecules to emit photons which have a frequency with integer multiples of the laser field [12]. The number of multiples is called the "order" of the high-harmonic pulse. The most common intuitive picture on generating higher order harmonics is based on a so-called three step model. This semi-classical description is composed of

i) ionization of an atom/molecule by tunneling of an electron to the continuum,

ii) acceleration of the free electron due to the laser field and returning to the parent ion and

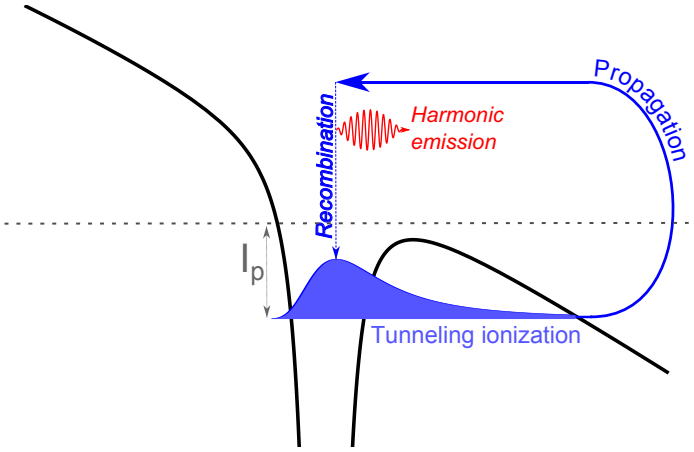

Figure 2.3: Semi-classical 3-step-model
(own illustration based on [11] and [3])

iii) recombination of the electron.

The process is illustrated in figure 2.3. If the trajectory of the free electron after the tunneling is considered classical, one can assume an electric field in the following form:

$$E(t) = E_0 \cos(\omega_0 t) \tag{2.10}$$

The classical Newtonian equation of motion reads as follows:

$$qE(t) = m\ddot{x}(t) \tag{2.11}$$

$$\Rightarrow \qquad \ddot{x}(t) = \frac{q}{m} E_0 \cos(\omega_0 t) \tag{2.12}$$

x denotes the propagation direction. Solving this differential equation through simple integration with $x(t_0) = 0$ and $\dot{x}(t_0) = 0$ leads to:

$$\dot{x}(t) = -\frac{E_0}{\omega_0}\frac{q}{m}\left[\sin(\omega_0 t) - \omega_0 \sin(\omega_0 t_0)\right] \tag{2.13}$$

$$x(t) = -\frac{E_0}{\omega_0^2}\frac{q}{m}\left[\cos(\omega_0 t) - \cos(\omega_0 t_0) + (\omega_0 t - \omega_0 t_0)\sin(\omega_0 t_0)\right] \tag{2.14}$$

For an electron the charge is $q = -e$. To simplify the equation $\Phi = \omega_0 t$ and $\Phi_0 = \omega_0 t_0$ are introduced:

$$x(t) = \frac{E_0}{\omega_0^2}\frac{e}{m}\left[\cos(\Phi) - \cos(\Phi_0) + (\Phi - \Phi_0)\sin(\Phi_0)\right] \tag{2.15}$$

The kinetic energy yields:

$$E_{kin} = \frac{1}{2} m\dot{x}(t)^2 \tag{2.16}$$

$$\Rightarrow \qquad E_{kin} = \frac{E_0^2}{\omega_0^2}\frac{e^2}{2m}\left[\sin(\Phi) - \sin(\Phi_0)\right]^2 \tag{2.17}$$

Figure 2.4: Gaussian intensity distribution of the beam (own figure)

The term $U_p = \frac{e^2 E_0^2}{4m\omega_0^2}$ is called "ponderomotive" energy of the laser field. Thus the kinetic energy of the electron can be written as:

$$E_{kin} = 2U_p \left[\sin(\Phi) - \sin(\Phi_0)\right]^2 \tag{2.18}$$

The phase of recombination can be obtained by solving the equation $x(\Phi_r) = 0$. The kinetic energy of the electron has a maximum at $\Phi_r = 255°$ and $\Phi_0 = 17°$ which means $E_{kin} = 3.17U_p$. With the ionization potential I_p the recombining electron emits a photon with an energy of $E_{kin}(\Phi_r) + I_p$. Therefore the highest possible energy of the generated high harmonics (which is called cutoff-energy) is the following [11]:

$$E_{cutoff} = 3.17U_p + I_p \tag{2.19}$$

High harmonics can be generated each half an optical cycle. For symmetry reasons there are only high harmonics of an odd order [3].

Phase matching

While the above discussion illustrates high-harmonics generation from a single atom or molecule, to achieve a photon flux, which can be used in the experiments, the radiation of many single emitters needs to be added. Therefore, a certain phase relation between the HHG photons emitted from different atoms needs to be fulfilled in order to ensure constructive interference between them. This condition is known as "phase matching". The laser beam has a cylindrical symmetry and in the ideal case a Gaussian intensity distribution as shown in figure 2.4. For higher harmonics generation the phase of the emitted photon is intensity dependent. Therefore photons emitted at different radii from the center of the beam have different phases. The pulse of higher harmonics is a coherent summation of all photons. This leads to constructive and destructive interference, which means that a larger length of the medium does not necessarily increase the photon flux [3]. The phase matching conditions are typically optimized by tuning the intensity of light, position and size of the laser focus and the density of emitting atoms.

2.4 Pump-probe method

A common approach to investigate molecular dynamics is the pump-probe method. A short laser pulse acts as a pump and excites the molecule or transfers it in a state of interest. The second laser pulse is the "probe" which brings the molecule in its final state to "view" the process. In ion momentum spectroscopy the probe pulse usually ionizes the molecule. The charged fragments can then be detected. The easiest realization of this method is to split up a pulsed laser beam with a beam splitter and then recombine them again. This way one part of the beam can be delayed by simply increasing the beam path on one side but not on the other. By using a delay stage the temporal delay and thus the evolution of the state of interest can be controlled and probed [3]. One often refers to two-color pump-probe studies if the pump pulse has a different wavelength than the probe pulse.

2.5 Kinetic energy release (KER)

In a dissociation or Coulomb-Explosion process the binding energy of a molecule is set free and carried away by the reaction fragments. The sum of the kinetic energies of all fragments is called kinetic energy release (KER) [13]. Thus the KER is calculated by

$$E_{KER} = \sum_{j=1}^{N} \frac{\vec{p_j}^2}{2m} \tag{2.20}$$

where N is the number of fragments.

2.6 Potential energies of O_2^+

Figure 2.5 shows low-lying potential energy curves for O_2^+ ions relevant for the experiments described here. The $\tilde{X}^2\Pi_g$ state is the ground state for O_2^+. A 11th harmonic photon of a 800 nm laser pulse lays above that level. Due to energy dispersion, in the experimental setup used for this work, the energy of one of those photons can vary between 17.0 eV and 17.5 eV [3]. This energy range touches the $\tilde{A}^2\Pi_u$ state, but can also populate the $a^4\Pi_u$ state. Both states are too low to reach the first dissociation channel of 18.733 eV, where a neutral O (^3P) and a positive $O^+(^4S^0)$-ion would be produced.

2.7 Gaussian beam

In the ideal case the laser pulse is a Gaussian beam, whose spatial and temporal profiles can be described in the following form:

$$\Phi(x) = \frac{1}{\sigma\sqrt{2\pi}} \cdot e^{-\frac{1}{2}(\frac{x}{\sigma})^2} \tag{2.21}$$

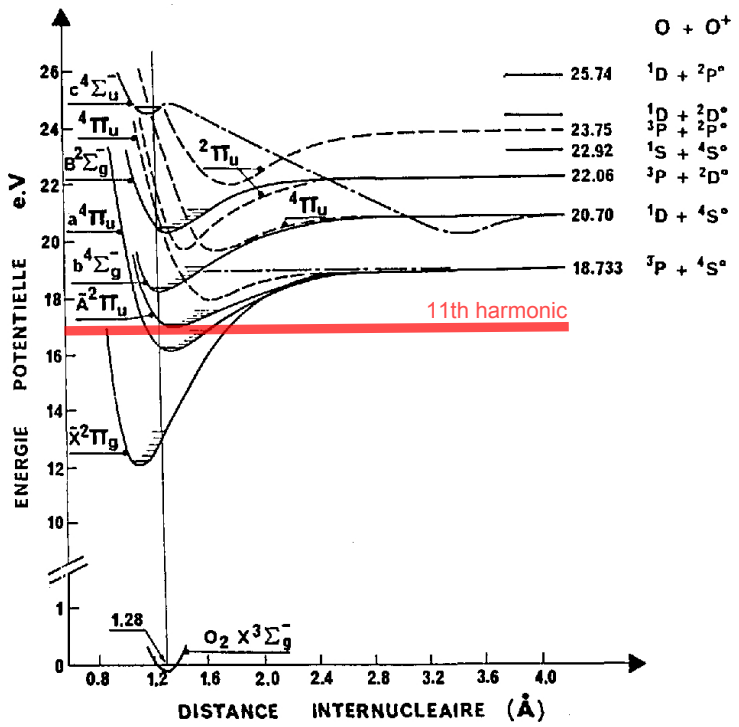

Figure 2.5: Potential curves for O_2^+ (modified from [2])

where σ is the standard deviation. When two of those beams are overlapping they form a convolution, which is in general given by [14]:

$$f(t) * g(t) = \int_{-\infty}^{\infty} f(u) \cdot g(t-u) du \tag{2.22}$$

According to the convolution theorem it is true that [14]

$$\mathfrak{F}(f(t) * g(t)) = \sqrt{2\pi} \cdot \mathfrak{F}(f(t)) \cdot \mathfrak{F}(g(t)) \tag{2.23}$$

Here $\mathfrak{F}$ is the Fourier transform of the function $f(t)$. Thus by plugging in $\Phi(t)$ one obtains:

$$\mathfrak{F}(f)(t) := \frac{1}{\sqrt{2\pi}} \cdot \int_{-\infty}^{\infty} f(x) e^{-itx} dx \tag{2.24}$$

$$\mathfrak{F}(\Phi)(t) = \frac{1}{\sqrt{2\pi}} \cdot \int_{-\infty}^{\infty} \frac{1}{\sigma\sqrt{2\pi}} \cdot e^{-\frac{1}{2}\left(\frac{x}{\sigma}\right)^2} \cdot e^{-itx} dx \tag{2.25}$$

$$= \frac{1}{2\sigma\pi} \cdot \int_{-\infty}^{\infty} e^{-\left(\frac{1}{2}\left(\frac{x}{\sigma}\right)^2 + itx\right)} dx \tag{2.26}$$

It is possible to complete the square via:

$$\frac{1}{2}\left(\frac{x}{\sigma}\right)^2 + itx = \left(\frac{1}{\sqrt{2}}\frac{x}{\sigma} + i\frac{\sqrt{2}t\sigma}{2}\right)^2 + \frac{1}{2}t^2\sigma^2 \tag{2.27}$$

Thus the Fourier transform of the Gaussian reads:

$$\mathfrak{F}(\Phi)(t) = \frac{1}{2\sigma\pi} \cdot \int_{-\infty}^{\infty} e^{-\left(\frac{x}{\sqrt{2}\sigma} + i\frac{t\sigma}{\sqrt{2}}\right)^2 - \frac{1}{2}t^2\sigma^2} dx \tag{2.28}$$

Now the substitution $\xi = \frac{x}{\sqrt{2}\sigma} + i\frac{t\sigma}{\sqrt{2}}$ is introduced with $dx = \sqrt{2}\sigma d\xi$:

$$\mathfrak{F}(\Phi)(t) = \frac{1}{\sqrt{2}\pi} \cdot e^{-\frac{1}{2}t^2\sigma^2} \int_{-\infty}^{\infty} e^{-\xi^2} d\xi \tag{2.29}$$

For the integral it is easily possible to calculate its square:

$$I := \int_{-\infty}^{\infty} e^{-\xi^2} d\xi \tag{2.30}$$

$$I^2 = \int_{-\infty}^{\infty} e^{-a^2} da \int_{-\infty}^{\infty} e^{-b^2} db = \int_{-\infty}^{\infty}\int_{-\infty}^{\infty} e^{-\left(a^2+b^2\right)} da\ db \tag{2.31}$$

$$\tag{2.32}$$

Converting the integral to polar coordinates by using $r^2 = a^2 + b^2$, $a = r\cos(\varphi)$ and $b = r\sin(\varphi)$ the surface differential becomes:

$$da\ db = dA = \det\left(\frac{\partial(a,b)}{\partial(r,\varphi)}\right) dr\ d\varphi = \begin{vmatrix} \cos(\varphi) & -r\sin(\varphi) \\ \sin(\varphi) & r\cos(\varphi) \end{vmatrix} dr\ d\varphi = r\ dr\ d\varphi$$

Thus the integral reads

$$I^2 = \int_0^{2\pi} d\varphi \int_0^{\infty} r \cdot e^{-r^2} dr = 2\pi \cdot \left[\lim_{r\to\infty}\left(-\frac{1}{2}e^{-r^2}\right)\right] + 2\pi \cdot \frac{1}{2} = \pi \tag{2.33}$$

$$\Rightarrow I = \sqrt{\pi} \tag{2.34}$$

and hence by using this result in equation 2.29 it is obvious that the Fourier transform of the Gaussian is again a Gaussian:

$$\mathfrak{F}(\Phi)(t) = \frac{1}{\sigma\sqrt{2\pi}} e^{-\frac{1}{2}t^2\sigma^2} \tag{2.35}$$

With the inverse Fourier transformation [14]

$$\mathfrak{F}^{-1}(f)(t) := \frac{1}{\sqrt{2\pi}} \cdot \int_{-\infty}^{\infty} f(x) e^{itx} dx \tag{2.36}$$

the convolution theorem 2.23 for two Gaussian functions can be evaluated:

$$\Phi_1(t) * \Phi_2(t) = \mathfrak{F}^{-1}\left(\mathfrak{F}(\Phi_1 * \Phi_2)\right)(t) \tag{2.37}$$

$$= \mathfrak{F}^{-1}\left(\sqrt{2\pi}\mathfrak{F}(\Phi_1)\mathfrak{F}(\Phi_2)\right)(t) \tag{2.38}$$

$$= \mathfrak{F}^{-1}\left(\frac{1}{\sigma_1^2\sigma_2^2\sqrt{2\pi}} e^{-\frac{1}{2}t^2\sigma_1^2} e^{-\frac{1}{2}t^2\sigma_2^2}\right)(t) \tag{2.39}$$

$$= \frac{1}{2\pi\sigma_1^2\sigma_2^2} \cdot \int_{-\infty}^{\infty} e^{itx} e^{-\frac{1}{2}(\sigma_1^2+\sigma_2^2)x^2} dx \tag{2.40}$$

As before one can again complete the square straight forward:

$$\frac{1}{2}\left(\sigma_1^2+\sigma_2^2\right)x^2 - itx = \left(\frac{\sqrt{\sigma_1^2+\sigma_2^2}}{\sqrt{2}}x - i\frac{\sqrt{2}t}{2\sqrt{\sigma_1^2+\sigma_2^2}}\right)^2 + \frac{t^2}{2(\sigma_1^2+\sigma_2^2)} \tag{2.41}$$

Thus the substitution is $\zeta = \left(\frac{\sqrt{\sigma_1^2+\sigma_2^2}}{\sqrt{2}}x - i\frac{\sqrt{2}t}{2\sqrt{\sigma_1^2+\sigma_2^2}}\right)$ with $dx = \sqrt{\frac{2}{\sigma_1^2+\sigma_2^2}}$. This leads to:

$$\Phi_1(t) * \Phi_2(t) = \frac{1}{2\pi\sigma_1^2\sigma_2^2} \frac{\sqrt{2}}{\sqrt{\sigma_1^2+\sigma_2^2}} \cdot e^{-\frac{1}{2}\frac{t^2}{\left(\sigma_1^2+\sigma_2^2\right)}} \int_{-\infty}^{\infty} e^{-\zeta^2} d\zeta \tag{2.42}$$

$$= \frac{1}{\sqrt{2\pi}\sigma_1^2\sigma_2^2\sqrt{\sigma_1^2+\sigma_2^2}} \cdot e^{-\frac{1}{2}\frac{t^2}{\left(\sigma_1^2+\sigma_2^2\right)}} \tag{2.43}$$

Therefore the convolution of two Gaussian beams is as well a Gaussian beam with a standard deviation of:

$$\hat{\sigma} = \sqrt{\sigma_1^2+\sigma_2^2} \tag{2.44}$$

2.8 Error propagation

For all experiments there is always an error in the measurements. One can distinguish between two different kinds of errors: systematic errors and statistical errors. Statistical errors are due to random fluctuations and proportional to $1/\sqrt{N}$, where N is the number of repetitions of the measurement [15]. Therefore the error gets smaller by repeating the experiment more often and is very high for low repetition rates. For the arithmetic average of a measured parameter x it is true that

$$\langle x \rangle = \frac{1}{N}\left(\sum_{i=1}^{N} x_i\right) \tag{2.45}$$

where N is the number of times, the parameter was measured. Its statistical error is given by the standard deviation [15]:

$$\sigma = \sqrt{\frac{1}{N-1}\sum_{i=1}^{N}(x_i - \langle x \rangle)^2} \tag{2.46}$$

The systematic error is, in the best case, only given by the accuracy of the used method of measurement and e.g. due to wrong gauging. Due to complex processes the uncertainty sometimes is unknown and has to be estimated. In case the measured data is processed and used in further calculations, the error has to be adapted. This kind of error propagation can be calculated by [15]:

$$\Delta f(x_1, ..., x_N) = \sum_{N}^{i=1} \left| \frac{\partial f}{\partial x_i} \right| \cdot \Delta x_i \tag{2.47}$$

Here f is a function with the parameters x_1 to x_N. Δx_i is the (estimated) error for the parameter x_i.

3 Experimental set up

The experimental set up was build by Wei Cao - a former PhD student at Kansas State University. The tabletop set up was modified to investigate time resolved molecular dynamics by using a pump-probe scheme. A laser beam is guided to the tabletop where it is sent to a beam splitter. One part of the beam goes to a delay stage and the other part goes to a semi-infinite gas cell. At this cell higher order harmonics are generated. The delayed IR pulse is then overlapped with the generated XUV pulse and guided to a ion momentum spectroscopy set up [3]. A schematic of the whole apparatus is shown in figure 3.1.

3.1 COLTRIMS set up

One of the state-of-the-art methods to analyse atomic and molecular dynamics is the Cold Target Recoil Ion Momentum Spectroscopy (COLTRIMS). In its interaction region a projectile beam (e.g. an ion or a laser beam) hits a cold target gas jet. The charged fragments are then accelerated by an electric field towards a detector, which have both, time and spatial resolution. In this case a delay-line detector is used, which consists of a micro channel plate and a delay-line anode. By using the time of flight and the spatial information from the detector signal one can trace back the trajectories of the charged particles. Thus it is possible to determine their initial momenta. In Wei Cao's set up, which is used in this work, the target gas jet is not cold. The gas is inserted in the chamber via a thin needle with a diameter of 1 mm. He decided to use an effusive gas jet to achieve a higher target density, because the XUV intensity of the HHG is too low to get satisfying results with a supersonic gas jet [3]. Therefore the initial transverse momentum spread is quite large. To avoid charging up the needle with ions or electrons of the interaction region, the needle has to be conductive and a needle voltage has to be applied to maintain the homogeneity of the electric field in the spectrometer [3].

3.1.1 Ion-electron-momentum Spectrometer

The spectrometer is basically composed of two detectors with a spatial resolution and a series of equidistant metal plates in between, which have a circular hole in the middle to allow particles to reach both detectors. The plates are connected via a resistor and a voltage is applied to the first and last plate to create a homogeneous electric field. Thus positive ions in the spectrometer are accelerated towards the detectors on the "short" side. It has a distance of 5.5 cm to the interaction region. The electrons are accelerated towards the "long" side, whose distance to the interaction region is 21 cm. To collect electrons from all directions a homogeneous magnetic field parallel to the electric field is applied via two Helmholtz-coils. Due

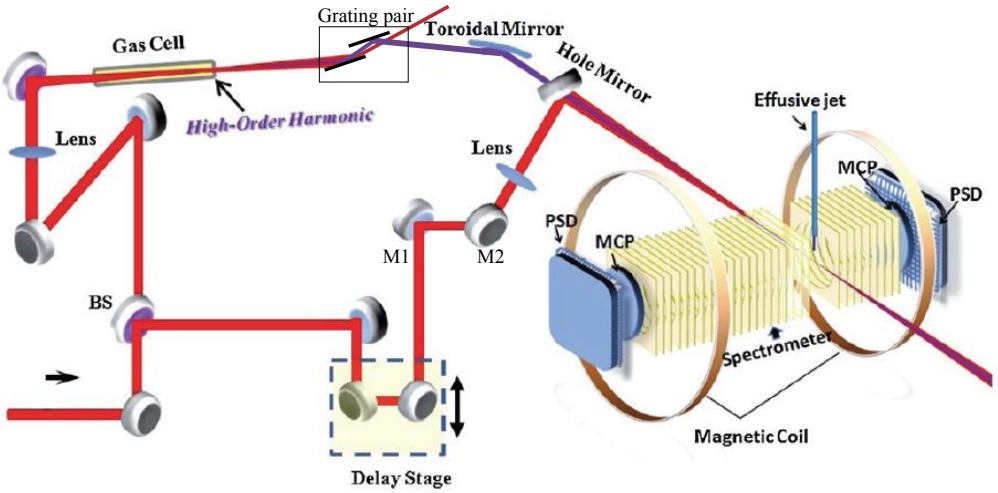

Figure 3.1: Sketch of the set up (modified from [3]). BS: beam splitter, PSD: position sensitive detector, MCP: micro channel plate, M1 and M2: mirrors to calibrate the spatial overlap between the XUV and IR beam.

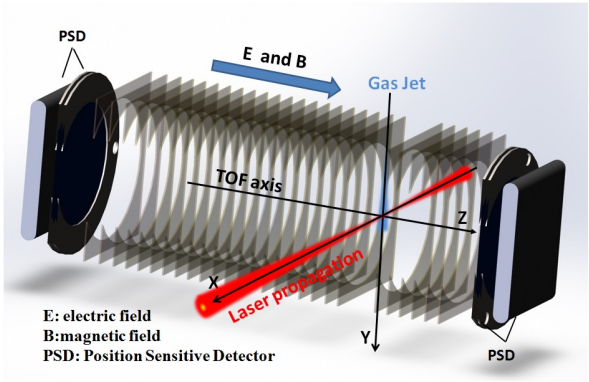

Figure 3.2: Sketch of the spectrometer (from [4])

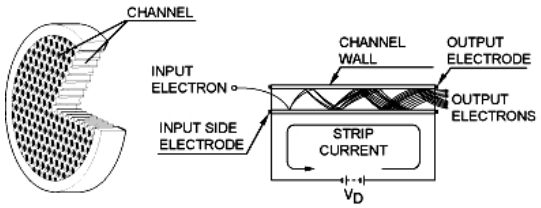

Figure 3.3: Sketch of a micro channel plate (from [4])

to the Lorentz force, the electrons are constrained on a spiral trajectory. Therefore even electrons with a high transverse momentum can reach the detector. A sketch of the spectrometer is shown in figure 3.2.

3.1.2 Micro Channel Plate (MCP)

For detecting charged particles it is necessary to amplify the amount of charges. A Micro Channel Plate (MCP) can be used for that purpose. It is made up of a lead glass plate equipped with many microscopic channels which have a diameter of a few microns. These channels are metallized with a high-impedance material. The front an back surfaces of the plate are metallized as well to apply a high voltage. A sketch is shown in figure 3.3. If an electron or an ion hits the wall inside a channel, secondary electrons will be emitted. These electrons will then be accelerated due to the high voltage and gain kinetic energy. Thus they will have enough energy to cause further avalanche electrons. This process will repeat until the avalanche electrons reach the end of the microscopic hole. At this time there will be a cloud of thousands of electrons, which can be detected (e.g. by a CCD camera or a Delay Line Anode) [4]. At the moment the avalanche of electrons escape the channel, the MCP will have a positive charge. This change of the potential can be measured at the front and back of the MCP which yields a fast time signal. The charge will be compensated by the applied voltage. The advantage of an MCP compared to other dynodes is the spatial restriction of the electron cloud. Thus the spatial information is conserved [16].

3.1.3 Delay Line Anode

Behind the MCP a two-layer Delay Line Anode is placed. It consists of a quadratic metal retainer with a ceramics insulator on its edges. Two parallel copper wires are winded around the retainer for each layer. There is a potential-difference of 50V [3] between the to wires, so the electrons are only hitting the more positive one, which is called the “signal” wire. The other one acts as a “reference” to subtract out possible errors. The signal is propagating with a constant speed in both direction of the wire as a high frequency signal according to the principle of the Lecher wire. Therefore the time sum of both signals is constant.

$$t_{sum,i} = (t_{i_1} - t_{MCP}) + (t_{i_2} - t_{MCP}) = const \tag{3.1}$$

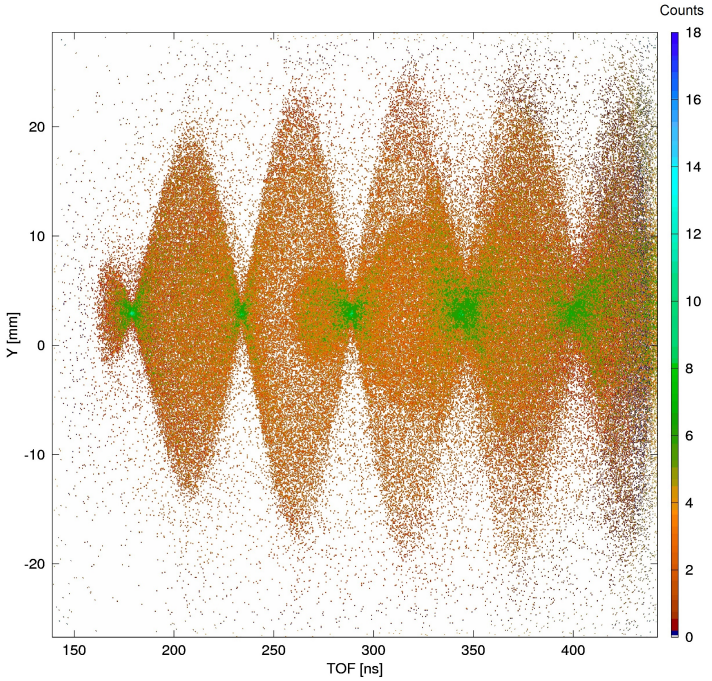

Figure 3.4: In the wiggle-spectra the time of flight is plotted vs. Y

Here i_1 and i_2 are the two wire tails in layer i and t_{MCP} is the time signal from the MCP. With the known time sum it is possible to determine the position [3]:

$$x = c_x(t_{x_1} - t_{x_2}) \tag{3.2}$$

$$y = c_y(t_{x_1} - t_{x_2}) \tag{3.3}$$

c_x and c_y are conversion constants. In Wei's set up the constants are $c_x = c_y = 0.5$ mm/ns.

3.1.4 Momentum and magnetic field calculations

Due to the homogeneous magnetic field there is a Lorentz force on the accelerated charged particles. This will force them on a cyclotron path. The cyclotron frequency can be calculated by looking at the equilibrium between the Lorentz force F_L and the centripetal force F_{cp}:

$$F_L = F_{cp} \tag{3.4}$$

$$|q|vB = \frac{mv^2}{r} \tag{3.5}$$

$$|q|B = m2\pi f \tag{3.6}$$

Here B is the magnetic flux density, q the charge of the particle and r the radius. For the velocity it is true that $v = \omega r = 2\pi f r$ where f is the cyclotron frequency. With equation 3.6 the magnetic field can be determined without knowing the applied current on the Helmholtz coils. For this a wiggle structure has to be analyzed, which

can be seen for electrons if the time of flight is plotted versus the X or Y detector image. An example of a wiggle-spectrum is shown in figure 3.4. Due to the projection of the circular motion on a 2D-plot, one can see knots every time the particle reaches the same position in the X- or Y-dimension. Thus the distance between two knots is one period $T = 1/f$ of the circular motion. With this the magnetic flux density can be determined:

$$B = \frac{2\pi m}{|q|T} \tag{3.7}$$

Once the magnetic field is known, the initial momenta can be calculated. the equation of motion is:

$$m \cdot \ddot{\vec{r}} = \vec{F} = \vec{F}_E + \vec{F}_L = q\left(\vec{E} + \vec{v} \times \vec{B}\right) \tag{3.8}$$

with the velocity $\vec{v} = (\dot{x}, \dot{y}, \dot{z})^T$ and the acceleration $\ddot{\vec{r}} = (\ddot{x}, \ddot{y}, \ddot{z})^T$. The magnetic and electric field both point in z-direction. Therefore their x- and y-components are zero. Thus the three components read:

$$\ddot{x} = \quad \frac{Bq}{m}\dot{y} \tag{3.9}$$

$$\ddot{y} = -\frac{Bq}{m}\dot{x} \tag{3.10}$$

$$\ddot{z} = \quad qE \tag{3.11}$$

The z-component can be solved by simple integration. Equations 3.9 and 3.10 are coupled second order differential equations. To solve them it is possible to use an ansatz like the following:

$$x(t) = A\cos(\omega t) + B\sin(\omega t) + C \tag{3.12}$$

$$x(t) = D\cos(\omega t) + E\sin(\omega t) + F \tag{3.13}$$

Here the short form $w = qB/m$ is used. Differentiating the ansatz yields:

$$\dot{x}(t) = -A\omega\sin(\omega t) + B\omega\cos(\omega t) \tag{3.14}$$

$$\dot{y}(t) = -D\omega\sin(\omega t) + E\omega\cos(\omega t) \tag{3.15}$$

$$\ddot{x}(t) = -A\omega^2\cos(\omega t) - B\omega^2\sin(\omega t) \tag{3.16}$$

$$\ddot{y}(t) = -D\omega^2\cos(\omega t) - E\omega^2\sin(\omega t) \tag{3.17}$$

By plugging in these equations in 3.9 and 3.10, one can see that the ansatz is only true for $B = D$ and $A = -E$. With the initial conditions $x(t = 0) = x_0$, $y(t = 0) = y_0$, $\dot{x}(t = 0) = v_x$ and $\dot{y}(t = 0) = v_y$ the solutions are:

$$x(t) = x_0 + \frac{v_y}{\omega} - \frac{v_y}{\omega}\cos(\omega t) + \frac{v_x}{w}\sin(\omega t) \tag{3.18}$$

$$y(t) = y_0 - \frac{v_x}{\omega} + \frac{v_x}{\omega}\cos(\omega t) + \frac{v_y}{w}\sin(\omega t) \tag{3.19}$$

$$z(t) = \frac{q}{2m}Et^2 + v_z t + z_0 \tag{3.20}$$

By solving this system of equations for v_y and v_x all the initial momenta are:

$$p_x = mv_x = \frac{m\omega}{2}\left[(x - x_0)\cot\left(\frac{\omega t}{2}\right) - (y - y_0)\right] \tag{3.21}$$

$$p_y = mv_y = \frac{m\omega}{2}\left[(y - y_0)\cot\left(\frac{\omega t}{2}\right) - (x - x_0)\right] \tag{3.22}$$

$$p_z = mv_z = \frac{(z - z_0)m}{t} - \frac{qE(t - t_0)}{2} \tag{3.23}$$

Due to the high mass of the positive ions, the magnetic field can be neglected. Thus the initial momenta for ions in x and y direction can be calculated easier:

$$p_x = mv_x = m\frac{(x - x_0)}{(t - t_0)} \tag{3.24}$$

$$p_y = mv_y = m\frac{(y - y_0)}{(t - t_0)} \tag{3.25}$$

3.2 Semi-infinite gas cell

There are different experimental approaches to generate higher harmonics, for instance waveguides and gas jets [17]. In this set up a semi-infinite gas cell (SIGC) was used. Since there is no jet nor a precast pinhole for the inlet or exit, the beam alignment is very easy and the pressure in the chamber is well known [17]. The cell is about 30 cm long and therefore much longer than the Rayleigh-length. This means that the whole focusing volume can be considered interaction region which leads to the name "semi-infinite" [3]. Thus the conversion rate can be higher than in many other approaches (in Wei's set up $\sim 10^{-6}$). The entrance for the IR pulse is covered by a window and the exit by a thin metal plate to keep up the pressure inside the chamber. By the time the IR pulse hits the thin metal plate, it drills a hole of about $200 - 300$ μm in it and enters the chamber, which is filled with a gas to generate higher harmonics.

3.3 Interferometer

By using an interferometer, the temporal overlap between the harmonics and the IR beam can be manipulated. It consists of a pair of mirrors mounted on a piezoelectric delay stage. The stage can be moved 90 μm electronically and 2 cm mechanically by hand. By reducing the distance between the stage and the other mirrors, the IR pulse comes earlier than before due to the shorter travel distance of the light. By moving the stage farther away, the IR comes later.

3.4 Grating

Before the XUV beam enters the spectrometer, it has to pass a pair of gratings. A sketch is shown in figure 3.5. This pair is used to select a single harmonic. Due to dispersion, the scattering of the light depends on the wavelength. Because the

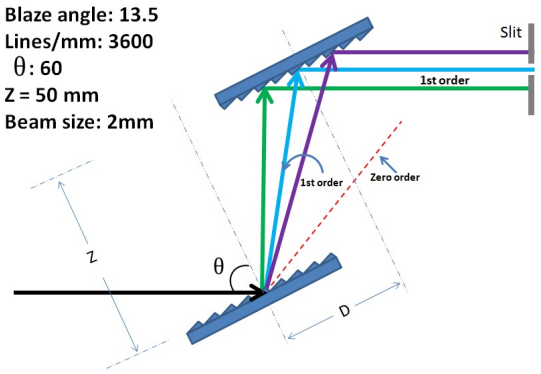

Figure 3.5: Sketch of the grating pair (from [3])

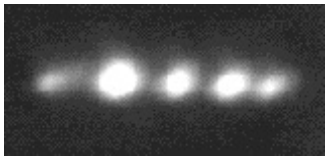

Figure 3.6: Higher harmonics as they appear on the phosphor screen in the spectrometer. From left to right: 9th, 11th, 13th, 15th, 17th harmonic

created harmonics have a discrete spectrum, it is possible to see the single harmonics and to select them, by moving the grating. A slit is used to block the unwanted harmonics. The residual infra red light is mostly scattered away. The XUV beam is then focused by a toroidal mirror. The beam can be viewed by a combination of a micro channel plate and a Phosphor screen. They are located a few centimeters behind the needle in the spectrometer. At the end of the spectrometer a CCD camera is placed and focused on the screen. This combination can be used as a beam viewer. In Figure 3.6 the grating slit is fully open. In that case it is possible to see 5 different harmonics at once with the beam viewer.

3.5 Signal Processing

The raw signal of the detectors can not be analysed directly. It has to be amplified and decoupled from the high voltage. Then the analogue signal is filtered and converted by a constant fraction discriminator (CFD) and a time to digital converter (TDC). After this process the digital signal can be processed by a data acquisition software [3]. For that purpose a software in SpecTcl was developed at the J. R. Macdonald laboratory. The whole process of signal processing is visualized in figure 3.7. A photodiode signal is used to serve as a “time zero” for all time of flight information. The photodiode is placed behind a mirror and detects transmission/scattering of the laser pulses.

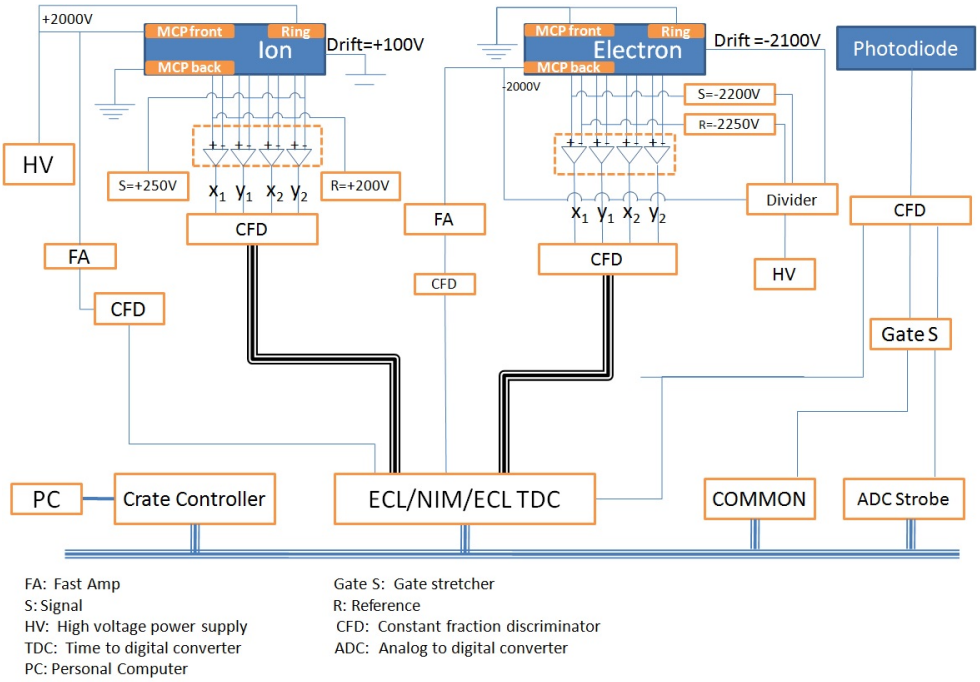

Figure 3.7: Visualization of the data acquisition system (from [3])

3.5.1 Constant Fraction Discriminator (CFD)

For precise timing information the analogue signal has to be processed, because the signals have different heights which leads to a variation in the timing information. Therefore the CFD splits up the signal, reverses one part and put both back together. This way a bipolar signal is created. Its zero-crossing is independent of the height. A zero-potential is needed to define this zero-crossing. Unfortunately it is not necessarily the ground potential. Thus adjusting the zero-potential changes the timing information. The error due to the "wrong" potential is called "walk". [18]

3.5.2 Time to Digital Converter (TDC)

After generating a time signal by the CFD a TDC is used to create a digital signal, which then can be processed by a PC. A simple way to measure the time is a capacitor. At the first time signal (time zero) the capacitor is charged up until the second hit, at which the discharging begins. Due to the fact that the charging current is constant, the charge is proportional to the time. Thus by "measuring" the charge, the time can be calculated [19].

4 Experiment

4.1 Calibration of the set up

For our experiments we requested beam time at the Kansas Light Source (KLS). This Laser facility can generate IR pulses with a duration between 8 fs and $\sim$ 45 fs [20]. We used 800 nm pluses of 35 fs with a repetition rate of 2 kHz. The experimental set up is located in a room next to KLS. Thus the beam has to go through a hole in the wall. Due to temperature differences in the two rooms there is airflow. Thus an enclosed tube is used to transport the beam from one tabletop to the other.

4.1.1 Beam alignment

Most mirrors are constructed to have a maximum reflection efficiency at an angle of 45°. Thus one should be very carefully with the beam alignment to keep the transmission loss as low as possible. Furthermore a large beam path is very sensitive to small deviations. The path should be kept horizontally at a constant height from the tabletop. This can be achieved by using irises for alignments. The beam could enter an iris perfectly centered even though it has a certain angle. Thus at least two irises are necessary.

4.1.2 Higher harmonics generation

In this set up higher harmonics were generated by a semi-infinite gas cell. Before each beam time we exchanged the exiting seal to guarantee a stable pressure inside the cell. Once the cell and the chamber are vented and the old seal is taken out, the focal spot should be adjusted. Due to ionization of the air it is possible to see

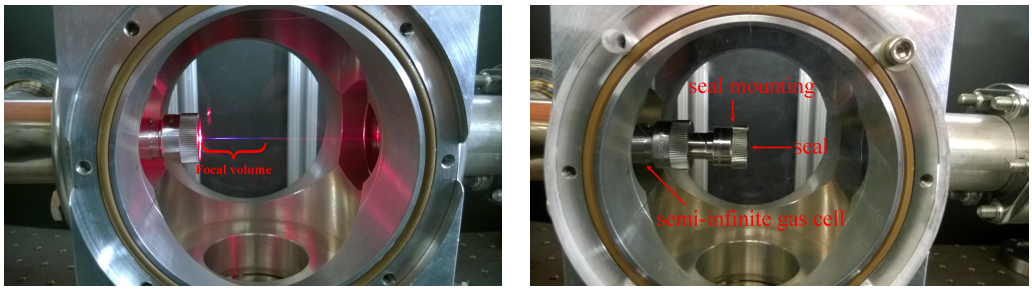

(a) The focal volume is visual in the vented chamber

(b) Sealed semi-infinite-gas cell

Figure 4.1: The focal spot position has to be adjusted to an optimal position within the gas cell

the focal volume by the naked eye as one can see in figure 4.1(a). Therefore the focal spot can be adjusted easily to fit inside the cell. Once the cell is checked for leakages, the chamber can be evacuated again. To generate higher harmonics we used Argon with a pressure of roughly 40 Torr for our experiments.

4.1.3 Overlap between the XUV pump and IR probe

In order to see two color effects the XUV and the IR beam have to overlap in space and time. In this set up the XUV path is "fixed" in the vertical direction. Thus most of the alignments have to be done with the IR path.

Spatial overlap

To get a rough spatial overlap the beam viewer (which was mentioned in chapter 3.4) can be used and the IR path can be blocked. For viewing the XUV path usually a voltage of 4 kV is applied to the phosphor screen and $1.2 - 2.0$ kV to the MCP. By moving the grating pair closer together or farther away, the harmonics beam can be shifted horizontally. This way different orders of higher harmonics can be selected. To determine the order of the harmonics it is useful to use Argon as a target in the spectrometer. For a 800 nm IR pulse the 9th harmonic has a photon energy of roughly 13.95 eV, but Argon an ionization potential of 15.76 eV [21]. Thus once one selected the 9th harmonic or lower orders, there are no Ar^+ counts in the spectrometer. The next higher harmonics, which is the 11th harmonic, has a photon energy around 17.3 eV. Therefore in case there are no Ar^+ counts, one just has to move the grating to get to the next higher harmonic until the counts dramatically increase. At this point the 11th harmonic is selected. Due to the fact that lower orders appear to the left and higher orders to the right on the screen, one can simply switch to the harmonic of interest. For adjusting the XUV beam to the intended interaction region, the needle can be lowered. If the beam is blocked by the needle, the path is crossing the interaction region. Once the XUV path is adjusted, the needle should be moved up about 1.5 mm. The IR path should never touch the needle, otherwise it might burn the nozzle. For the spatial overlap the XUV position on the beam viewer can be marked with a cross in the software XCAP. For viewing the IR beam an attenuator has to be used to prevent the MCP from getting burned. By adjusting the last "outside of vacuum" mirror before the beam enters the spectrometer, one can fit the beam path to the cross-marking in XCAP. This is only a rough method, because the beam viewer is a few centimeters behind the interaction region. A second way for adjusting the beams is by looking at the time of flight for some ions with XUV only and IR only. Obviously a gas which can be ionized by both, the IR beam itself and XUV beam itself should be used. The time of flight depends on the position in z-direction. Thus the IR path can be adjusted horizontally to match the TOF one obtains with XUV only. For the vertical adjustment the detector image in X-Y-direction is a possible tool by using the same principle. This method is not that reliable i.a. due to the effusive jet. However, a combination of both methods can be used to make the XUV and IR beam collinear. The TOF and detector image represent a first reference point, because they depend on the alignment directly in the interaction region, which is underneath the needle.

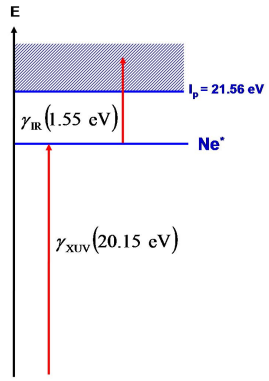

Figure 4.2: Energy schematics of neon (own illustration)

This reference should be adjusted by the mirror "M2" (see figure 3.1). Mirror "M1" could then be used to adjust the spatial overlap at the beam viewer, which acts as a second reference point. By doing multiple iterations of this method, the beams will eventually become collinear.

Temporal overlap

Once the spatial overlap is optimized, finding the temporal one is heuristical. One should use a target gas that shows two color effects in the intended energy region. One example is neon, which has an ionization potential of 21.56 eV [21]. One photon of the 13th harmonic (assuming a 800 nm driving field) with roughly 20.15 eV is not enough to produce Ne^+, but it can induce an excited state Ne^*. Thus at least one photon of the IR-pulse (1.55 eV) is needed for ionization. If the XUV-pulse comes first and then the IR-pulse Ne^+ is produced. If IR comes first, there are almost no neon-ions in the spectrometer. Thus the delay stage can be moved manually step by step to find the transition region. The delay scan for neon is described below.

4.2 Two-color delay scan of neon

For our two-color delay scan of neon we used the KLS laser with a pulse duration of 35 fs and a wavelength of 800 nm. The XUV-beam was linearly polarized in y-direction (in the detector plane) and the IR linearly in the direction of the time of flight. As mentioned before neon has an ionization potential of 21.56 eV, but one photon of the 13th harmonic has only roughly 20.15 eV. One extra photon of the IR-pulse is enough to ionize neon. Heuristically we found the transition region and did a delay scan with a range of 300 fs. Unfortunately at this time we used a different software for the delay stage, which used only roughly half of its full range. Nevertheless we could capture the full transition region.

4.2.1 Determination of the pulse duration

In figure 4.3 we plotted the normalized count rate versus the delay. Here the 0 fs delay does not necessarily mean, that XUV and IR are perfectly overlapping in the

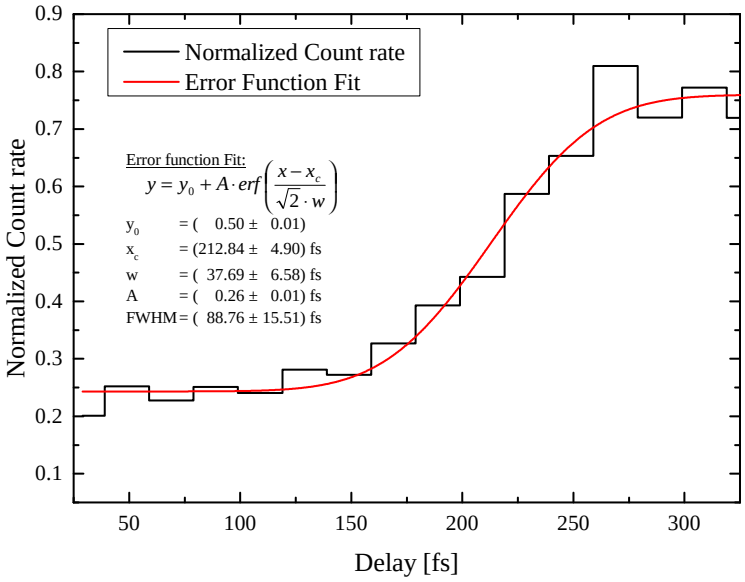

Figure 4.3: Two-color delay scan of neon

time domain. The larger the delay, the later the IR compared to the XUV beam. It is useful to normalize the counts with respect to an ion, which shows no delay-dependence. In this example water is a suitable candidate, since it almost always appears in the background with a more or less constant contribution. Compared to the range of the delay stage, the lifetime of the exited neon state is very long. Thus the transition region is expected to appear like a blured out step-function, although both beams (IR and XUV) are assumed to be Gaussian. This step-function-like shape can be described by an integrated Gauss function, which is called error-function. Therefore we used this function for fitting the data. The full width at half maximum yields (88.76 ± 15.51) fs. The pulse duration can be obtained by using the standard deviation of the convolution as described in chapter 2.7. According to equation 2.44 it is true that $\hat{\sigma} = \sqrt{\sigma_{IR}^2 + \sigma_{XUV}^2}$. Since we know the pulse duration of the IR-beam and obviously $\hat{\sigma} = (88.76 \pm 15.51)$ fs, the pulse duration of the 13th harmonic is:

$$\sigma_{XUV} = \sqrt{\hat{\sigma}^2 - \sigma_{IR}^2} = \sqrt{(88.76 \text{ fs})^2 - (35 \text{ fs})^2} \pm \Delta\hat{\sigma} = (81.57 \pm 19.02) \text{ fs} \quad (4.1)$$

The error was calculated according to equation 2.47 by assuming a deviation of 5 fs for the IR pulse:

$$\Delta\sigma_{XUV} = \left|\frac{\partial\sigma_{XUV}}{\partial\hat{\sigma}}\right| \cdot \Delta\hat{\sigma} + \left|\frac{\partial\sigma_{XUV}}{\partial\sigma_{IR}}\right| \cdot \Delta\sigma_{IR} \quad (4.2)$$

$$= \frac{\hat{\sigma}}{\sqrt{\hat{\sigma}^2 - \sigma_{IR}^2}} \cdot \Delta\hat{\sigma} + \frac{\sigma_{IR}}{\sqrt{\hat{\sigma}^2 - \sigma_{IR}^2}} \cdot \Delta\sigma_{IR} \quad (4.3)$$

4.3 XUV-IR delay scan of molecular oxygen

For O_2 we recorded data for higher and lower voltages. With higher voltages the analysis for ions becomes easier. The peaks for different ions are more separated in the time domain. For electron analysis a lower voltage is more appropriate to get a higher resolution. A higher voltage would mean, that the electrons gain more speed in z-direction. The x- and y-velocities should not be effected. This is why at high voltages the electrons could not accomplish many cycles of a cyclotron period, which would result in an impractical wiggle-spectrum. However, the ion-spectra are still acceptable for low voltages.

4.3.1 Determination of the magnetic field

To determine the magnetic field we applied no spectrometer voltage in order to see many wiggles. The spectrum is plotted in figure 3.4. The distance between two wiggles is (61 ± 1) ns. With equation 3.7 the magnetic flux density is $B = (5.856 \pm 0.096) \cdot 10^{-4}$ T $= (5.856 \pm 0.096)$ Gs. This value was used for the momenta and energy calculations.

4.3.2 Pump-probe experiments

The time of flight of a particle is proportional to the square root of its mass over charge ratio. Thus by identifying just one ion peak, all the other peaks can be predicted via:

$$TOF_j = TOF_i \cdot \sqrt{\frac{m_j \cdot |q_i|}{m_i \cdot |q_j|}} \tag{4.4}$$

TOF_i is the time of flight of ion i, m_i its mass and q_i its charge. The index j stands for particle j, whose TOF is intended to be calculated. As for neon we used the KLS laser with 35 fs IR pulses to do experiments on O_2. The time of flight spectrum for IR only is shown in figure 4.4(a). There are H_2O^+ and OH^+ peaks, which come from the background. Obviously there is no O^+ produced here, which should show up at a TOF of roughly 4000 ns. With the IR pulse, O_2 can be ionized due to a multi-photon process. But for dissociation, even more photons are necessary. The intensity of the IR-beam (estimated to be of order of $\sim 10^{13}$ W/cm^2) is not high enough to do so. We recorded the same spectrum again with the XUV-beam only. As mentioned in chapter 2.6, the 11th harmonic has enough energy to ionize O_2 but not enough to dissociate it. This is why in figure 4.4(b) there is almost no peak for O^+ in the TOF spectra. However, there might be very few counts due to second order diffraction of the grating pair. The 11th harmonic would overlap with the 22nd harmonic. Because there are only odd orders of harmonic, there are the second order diffraction 21st and 23rd harmonic very close in spatial domain to the first order 11th harmonic. Fortunately the efficiency of the grating pair for second order diffraction is very low [3].

After knowing the spectra for single colors, we did an XUV-IR delay scan. The time of flight spectrum is shown in figure 4.5. Here the spectrum is integrated over

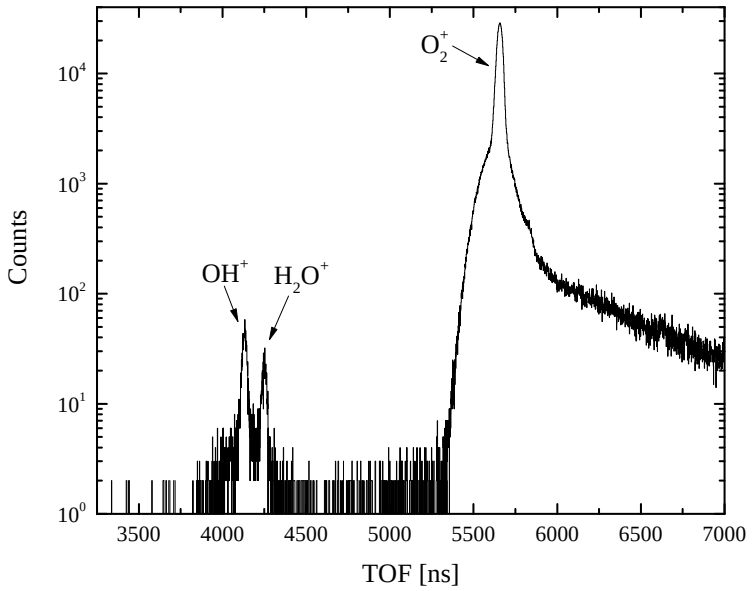

(a) Time of flight for IR only

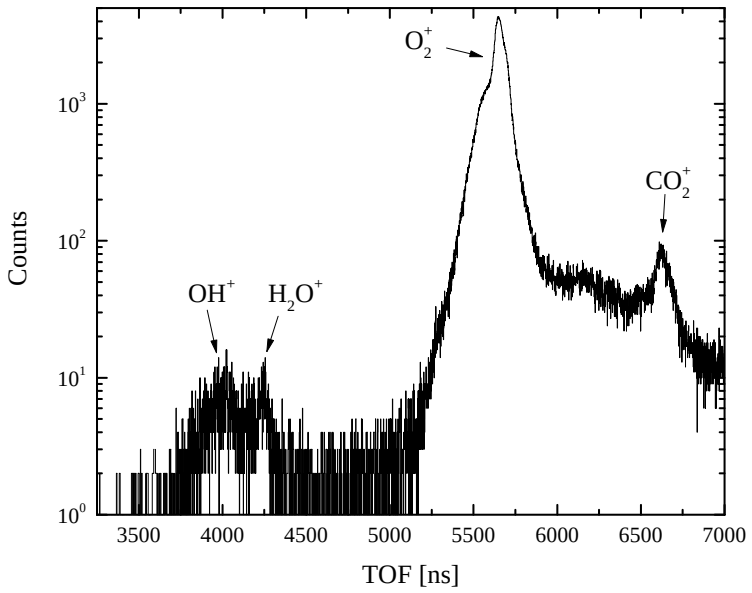

(b) Time of flight for XUV only

Figure 4.4: Time of flight spectra for O_2 with one color only.

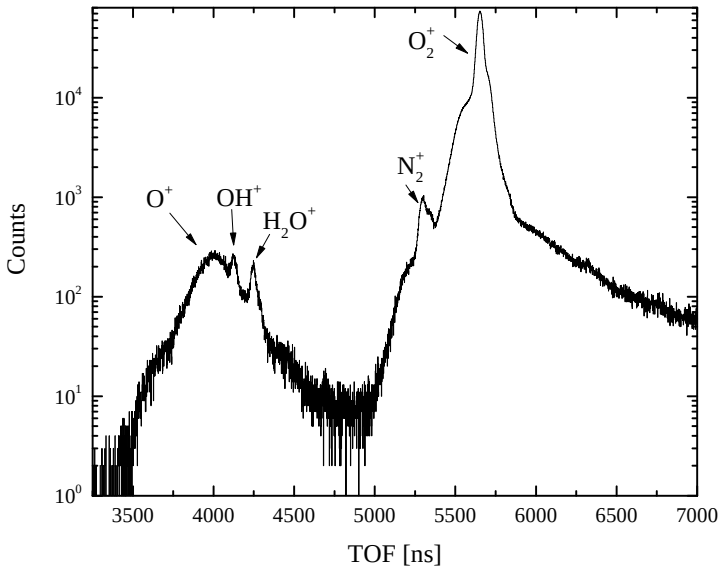

Figure 4.5: TOF spectrum for O_2 (XUV + IR) integrated over an IR delay from -370 to 230 fs. For the XUV-pump the 11th harmonic was used.

a delay scan from -370 to 230 fs. Here we can clearly see a O^+ peak. Figure 4.6 shows the region of the time-of-flight spectrum as a function of Y-position on the detector. The plot is zoomed in on the dissociation channel. This spectrum reflects the (linearly) scaled two-dimensional momentum distribution of O^+ ions. One can clearly see an outer and an inner ring of O^+-ions, which corresponds to higher or lower energetic ions, respectively. One can also see the peaks of H_2O^+ and OH^+. This background is subtracted in further considerations (especially for momenta and energy calculations).

In figure 4.7(a) the normalized count rates for O_2^+-ions and O^+-ions are plotted versus the delay of the IR-pulse. One can clearly see that there is a delay-dependence in the O^+ yield. There are roughly 2.8 times more counts at a delay stage position of 0 fs compared to the -370 fs position, where the IR-pulse comes earlier than the XUV-pulse. The same applies if one looks at figure 4.7(b) where the count ratio of O^+/O_2^+ is plotted. This delay dependence looks similar to our neon measurement with the 13th harmonic. Thus we tried the same error function fit for the oxygen data, which is also shown in figure 4.7(b). Here we obtained for the full width of half maximum (124.0046 ± 7.5316) fs. In figure 4.7(a) a delay-dependence of the IR-induced high energy sideband in the measured electron spectrum is also plotted. If only one XUV photon is absorbed by O_2, the emitted electron cannot have more energy than $h\nu_{XUV} - I_p$. For O_2 the ionization energy is $I_p \approx 12.07$ eV [21]. Therefore the electron from an XUV-only process is not able to have more energy than 5.45 eV. In case the molecule absorbs/emits additionally N IR-photons the electron energy is given by $h\nu_{XUV} - I_p \pm N \cdot h\nu_{IR}$. These peaks are called sidebands. By looking

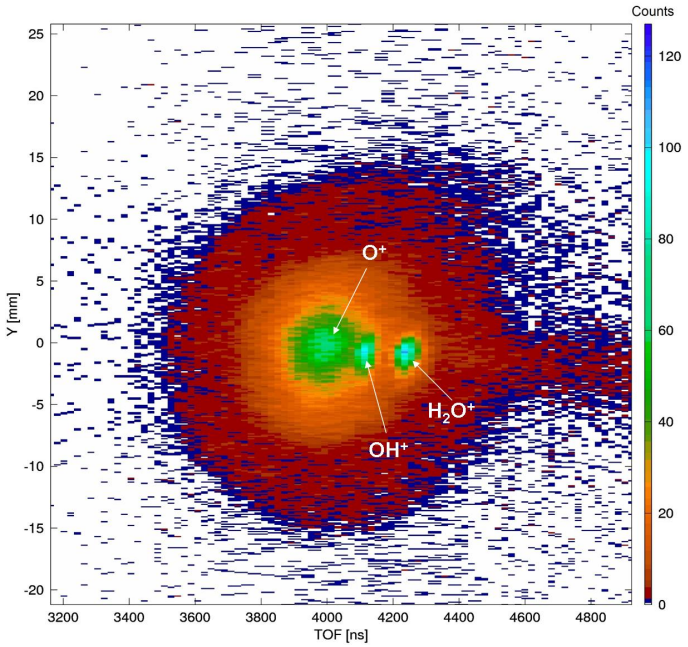

Figure 4.6: Time of flight versus Y integrated over an IR delay from −370 to 230 fs.

only at electrons with more than 6 eV we could find one of those sidebands. In the delay domain, it has its maximum as expected at the steep slope of the O^+-yield where the XUV- and IR-pulse are overlapping in space and time. Thus, the delay-dependence of the sideband yild reflects the cross correlation between the XUV and IR pulses [3]. The peak position of the sideband was used to determine the "zero"-delay between XUV and IR for all plots in chapter 4.3.2. All experiments discussed here were done with an linear IR polarization in z-direction (i.e. TOF direction) and XUV in y-direction. Anyhow, we found the same results for IR polarized in the same direction as XUV.

The O^+ energy is plotted versus the IR-XUV-delay in figure 4.8. One can see that there is a lower energy-band between 0 eV and roughly 0.3 eV and a higher energy-band between 0.3 and 1.25 eV. This energies correspond to the "inner" or "outer" dissociation ring, respectively in figure 4.6. Both energy-bands show a clear delay-dependence. They are both projected on the delay-axis in figure 4.9(b). For the higher energy-band the corresponding ion counts increase very steeply in the overlapping region (around 0 fs delay). It reaches its maximum counts between 50 fs and 90 fs delay. Therefore O^+ ions with an energy between roughly 0.3 and 1.25 eV only appear in the direct overlapping region in the time domain. This indicates, that the XUV and the IR photon are absorbed almost simultaneously for these higher energies. However, the counts for the lower energy-band seem to rise slower and then stay flat at their maximum value. This shape implies, that these O^+ ions are produced as soon the IR-pulse comes later than the XUV-pulse. This feature is confirmed by the energy projections in figure 4.9(a). For the first projection between −370 and −290 fs, the O^+-ions mainly have low energies. Between −60 and 30 fs a tail towards higher energies is appearing, which corresponds to the higher

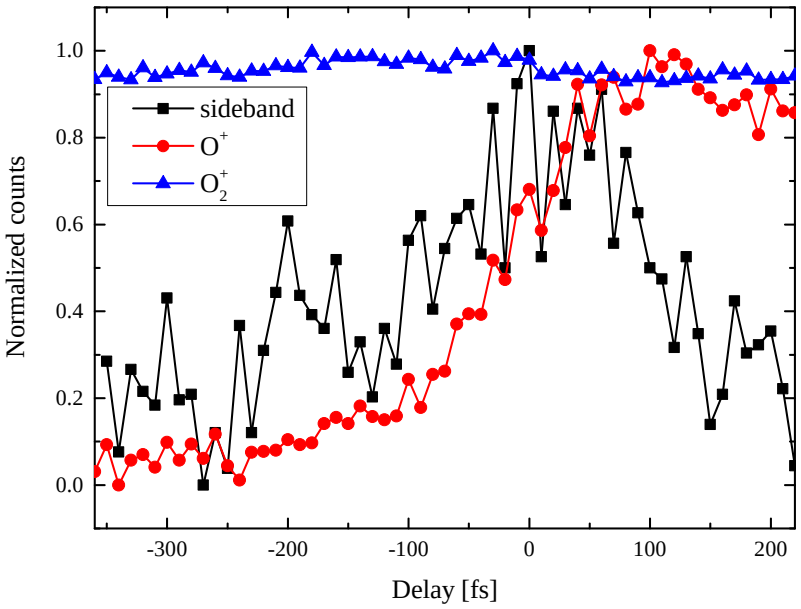

(a) Normalized count rates for O^+, O_2^+ and the electron sideband

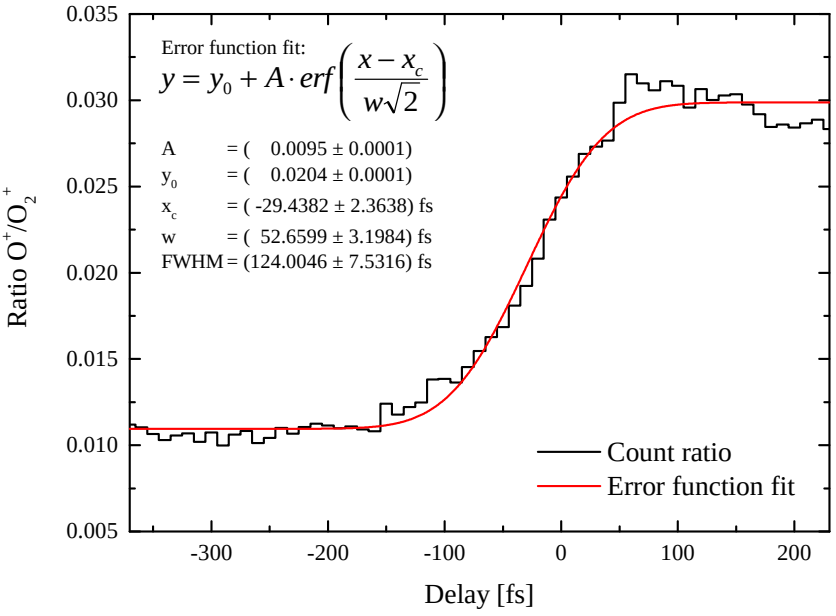

(b) Count ratio of O^+/O_2^+

Figure 4.7: XUV-IR delays scan on O_2

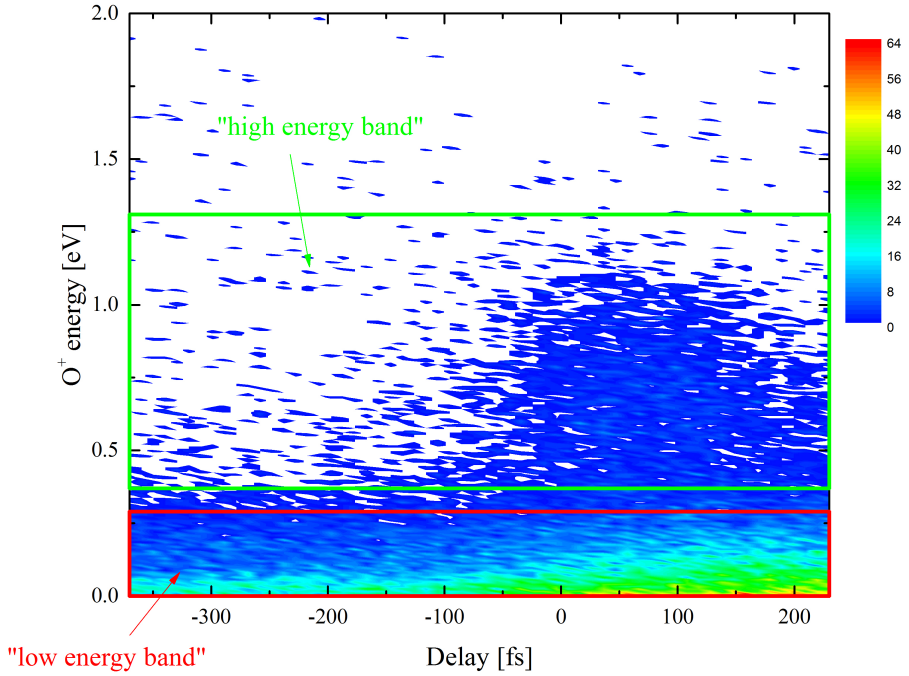

Figure 4.8: O^+ energies vs. delay

energy-band in the overlap region. In the 160 to 230 fs projection, this tail starts to disappear again, which means that for larger delays, the O^+ energy spectrum is dominated by lower energies. Due to the fact that both effects form a convolution, the yield of O^+-ions in figure 4.7(b) can be explained. The slope between -150 and 50 fs is simply amplification due to the rising count rates in both, the higher and the lower energy-band. At delays above 100 fs the O^+ yield does not stay constant, because the counts at the higher energy band start to drop down. This causes a short decrease of the overall O^+ yield until it really stays flat. The higher energy band lies in a region, that implies that for this process at least one more IR-photon has to be absorbed compared to the low energy-band. One IR photon has an energy of 1.55 eV. All the ion energies in the mentioned plots have to doubled, because in the dissociation channel one fragment is neutral and therefore not detected. Due to momentum conservation, both fragments have the same initial kinetic energy. By doubling the energies, one can see that the distance between the main peaks of the lower and higher energy-band is roughly 1.55 eV.

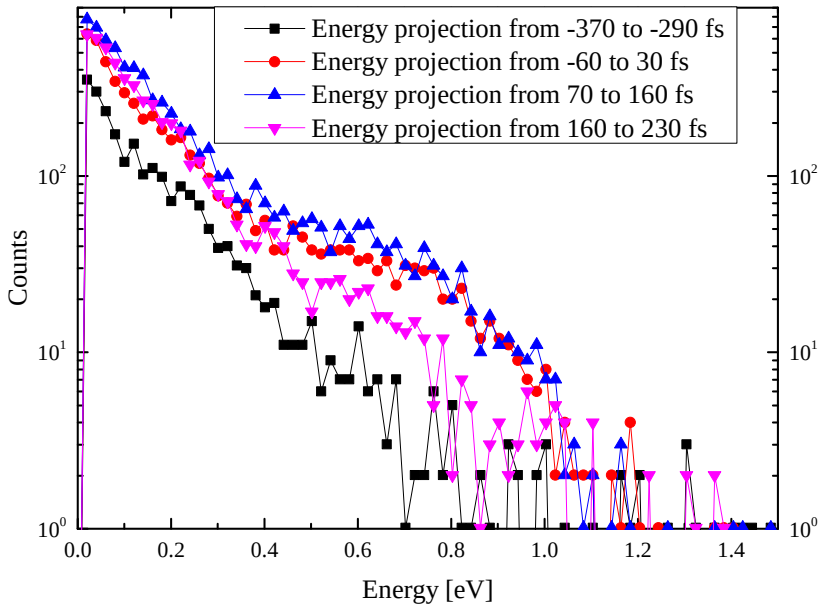

(a) O^+ energy projections

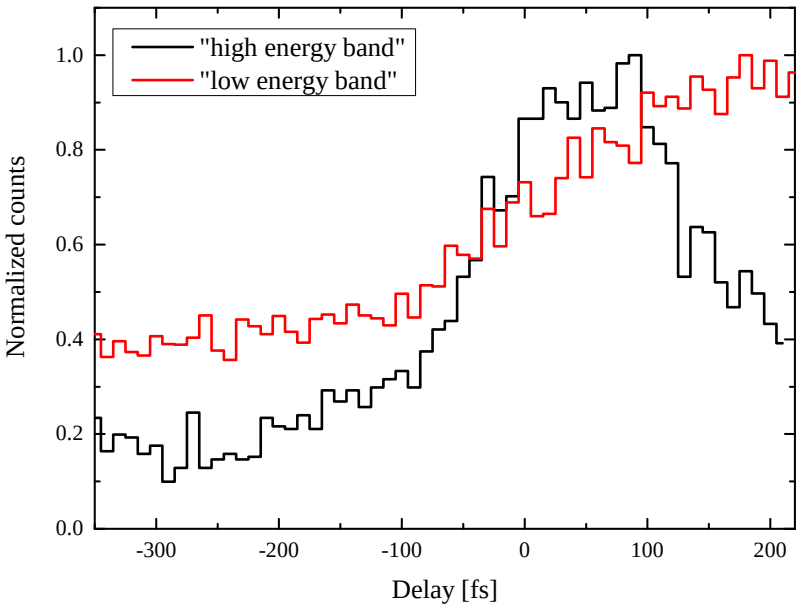

(b) Delay projections of O^+ energies between 0 and 0.3 eV 0.36 and 1.31 eV

Figure 4.9: Energy and delay projections of O^+

5 Conclusion and outlook

In this work 35 fs, 800 nm laser pulses of the Kansas Light Source were used to generate higher order harmonics, which were sent through a pair of gratings to select a single harmonic out of a broad XUV spectrum. The created 11th harmonic, synchronized with its fundamental IR laser pulse, was used for pump-probe experiments on molecular oxygen fragmentation. The harmonic pulse created an O_2^+ molecular ion, which was then dissociated with the IR pulse. The reaction products were characterized using recoil ion and electron momentum spectrometer. The 11th harmonic mostly populated the $A^2\Pi_u$ ionic state by a nearly resonant transition from the ground state of a neutral molecule, thus, resulting in a very low-energy electron ($0 - 0.2$ eV). Two different dissociation channels of the created O_2^+ ions were found, corresponding to the net absorption of one or two IR photons (similar to well known "1ω" and "2ω" pathways in IR dissociation of the H_2^+ molecular ions [e.g., Thompson et al. [22]; Walsh et al. [23]]). The low energy channel originates from a single photon transition to a $f^4\Pi_g$ dissociative state, resulting in O^+ ions with energies just above the dissociation threshold. One photon coupling between these two states can be reached in a broad range of internuclear distances, resulting in the nearly constant yield of this channels for all delays where the IR pulse arrives later than the XUV. On the other hand, the KER for the higher-energy channel (~ 1.5 eV) indicates that it is most likely produced by the dissociation via the same state reached at smaller internuclear distance involving the absorption of an additional 1.5 eV IR photon. Because of the symmetry of the states involved, this is most likely a three-photon transition with a subsequent stimulated emission of one photon ("net" two-photon absorption, similar to "2ω" channel for H_2^+ [Walsh et al. [23]]). Because the three-photon coupling is reached at the left (steep) side of the $A^2\Pi_u$ potential well close to the equilibrium distance of the neutral (see figure 5.1 - new pot. curves modified from Magrakvelidze et al. [5])), this channel is mostly populated only within a short time window after the XUV pulse, which is reflected in a fast decrease of its yield with decreasing delay (see figures 4.8, 4.9(b)).

The above interpretation of the results is preliminary, and more detailed data analysis is underway. The JRML group plans to compare the experimental results with the simulations similar to the one presented in [Magrakvelidze et al. [5]] but updated for the case of XUV pump pulses. These experiments also show considerable potential for this type of pump-probe experiments for molecular dynamics studies. The key point here is the selection of a single harmonic, which allows for a selective population of a single molecular state. This experimental arrangement can be applied to study a broad range of molecules, and the first experiments on D_2 and CO_2 were performed in parallel with the measurements reported here [D. Trabert, bachelor thesis, in preparation].

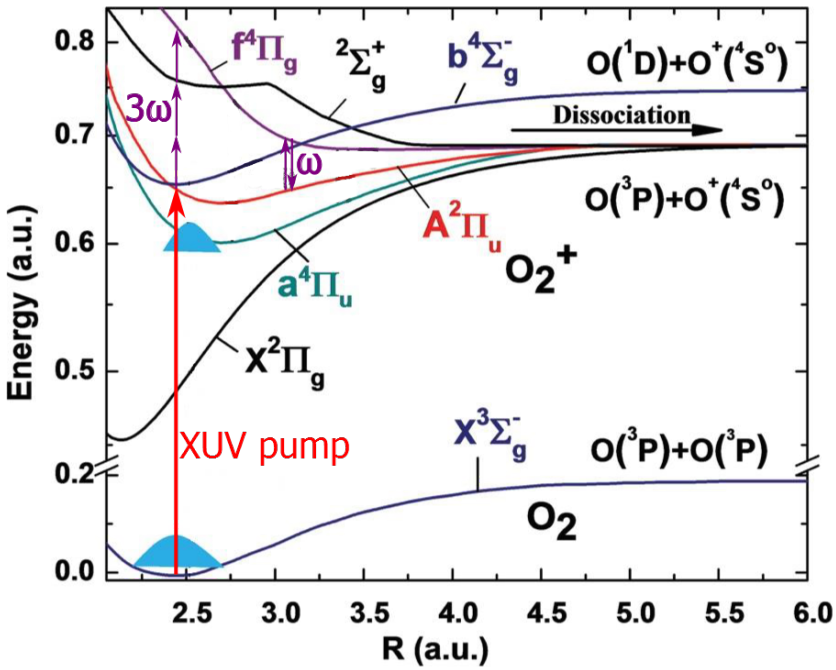

Figure 5.1: Potential curve for O_2^+ (modified from [5])

Bibliography

[1] Z. Deng and J. H. Eberly, J. Opt. Soc. Am. B **Vol. 2, No. 3**, 486 (1985), URL http://www.opticsinfobase.org/josab/abstract.cfm?URI=josab-2-3-486.

[2] P.-M. Guyon and I. Nenner, Appl. Opt. **19**, 4068 (1980), URL http://ao.osa.org/abstract.cfm?URI=ao-19-23-4068.

[3] W. Cao, *Dissertation on »pump-probe study of atoms and small molecules with laser driven high order harmonics«* (2014).

[4] D. M. P. Inc., *Microchannel Plates @ONLINE*, http://www.dmphotonics.com/MCP_MCPImageIntensifiers/microchannel_plates.htm (2014).

[5] M. Magrakvelidze, C. M. Aikens, and U. Thumm, Phys. Rev. A **86**, 023402 (2012), URL http://link.aps.org/doi/10.1103/PhysRevA.86.023402.

[6] C. Mortimer and U. Müller, *Chemie: das Basiswissen der Chemie ; 126 Tabellen* (Thieme, 2007), ISBN 9783134843095.

[7] W. Demtröder, *Experimentalphysik 3: Atome, Moleküle und Festkörper; 4. Aufl.*, Springer-Lehrbuch (Springer, Berlin, 2010).

[8] D. J. Griffiths, *Introduction to Electrodynamics* (Pearson, San Francisco, CA, 2008).

[9] J. D. Jackson, *Classical electrodynamics* (Wiley, New York, NY, 1999), 3rd ed., ISBN 9780471309321, URL http://cdsweb.cern.ch/record/490457.

[10] G. Mainfray and G. Manus, Reports on Progress in Physics **54**, 1333 (1991), URL http://stacks.iop.org/0034-4885/54/i=10/a=002.

[11] K. L. Ishikawa, *High-Harmonic Generation, Advances in Solid State Lasers Development and Applications, Mikhail Grishin (Ed.)* (InTech, 2010), ISBN 978-953-7619-80-0,.

[12] M. Lewenstein, P. Balcou, M. Y. Ivanov, A. L'Huillier, and P. B. Corkum, Phys. Rev. A **49**, 2117 (1994), URL http://link.aps.org/doi/10.1103/PhysRevA.49.2117.

[13] Y.-C. Chiang, F. Otto, H.-D. Meyer, and L. S. Cederbaum, The Journal of Chemical Physics **136**, 114111 (2012), URL http://scitation.aip.org/content/aip/journal/jcp/136/11/10.1063/1.3694536.

[14] L. Papula, *Mathematik Für Ingenieure und Naturwissenschaftler Band 2*, Mathematik für Ingenieure und Naturwissenschaftler (Vieweg Verlag, Friedr, & Sohn Verlagsgesellschaft mbH, 2011), ISBN 9783834886439.

[15] H. Ku, J Research of National Bureau of Standards-C. Engineering and Instrumentation **70C, No. 4**, p. 263 (1966), URL http://nvlpubs.nist.gov/nistpubs/jres/70C/jresv70Cn4p263_A1b.pdf.

[16] L. P. H. Schmidt, S. Schößler, A. Czasch, O. Jagutzki, and R. Dörner, *Microchannel plate (MCP) detectors @ONLINE*, https://www.atom.uni-frankfurt.de/research/coltrims/mcp/ (2014).

[17] D. S. Steingrube, T. Vockerodt, E. Schulz, U. Morgner, and M. Kovačev, Phys. Rev. A **80**, 043819 (2009), URL http://link.aps.org/doi/10.1103/PhysRevA.80.043819.

[18] K. Carnes, *James R. Macdonald Laboratory, Constant Fraction Discriminators @ONLINE*, http://jrm.phys.ksu.edu/Resource/Pubs/CFD/CFD.html (2003).

[19] J. Kalisz, Metrologia **41**, 17 (2004), URL http://stacks.iop.org/0026-1394/41/i=1/a=004.

[20] V. Needham, *James R. Macdonald Laboratory, KLS @ONLINE*, http://jrm.phys.ksu.edu/lasers.html (2014).

[21] U.S. Department of Commerce - National Institute of Standards and Technology, *Nist atomic spectra database @ONLINE*, http://www.nist.gov/ (2014).

[22] M. R. Thompson, M. K. Thomas, P. F. Taday, J. H. Posthumus, A. J. Langley, L. J. Frasinski, and K. Codling, Journal of Physics B: Atomic, Molecular and Optical Physics **30**, 5755 (1997), URL http://stacks.iop.org/0953-4075/30/i=24/a=014.

[23] T. D. G. Walsh, F. A. Ilkov, and S. L. Chin, Journal of Physics B: Atomic, Molecular and Optical Physics **30**, 2167 (1997), URL http://stacks.iop.org/0953-4075/30/i=9/a=017.

Appendix

Software in use

Mathematica 8
Computational Software. It was used for plotting and modifying illustrations.

OriginLab 9.1
Analysis and plotting software.

SpecTcl
GUI builder for Tcl/Tk (Tool command language). The data acquisition software was written in SpecTcl. Thus it was used to record, analyse and plot data on the fly.

InkScape
This vector graphics editor was used for drawing and modifying illustrations.

LabView 11
Laboratory Virtual Instrument Engineering Workbench. LabView was used to control the delay stage

XCAP
Image Analysis Software for PIXCI® Frame Grabbers. This software was used for the beam viewer.

LaTeX 2ε
The document markup language was used to write this thesis.

Selbstständigkeitserklärung

nach § 28 (12) der Ordnung des Fachbereichs Physik an der Johann Wolfgang Goethe-Universität für den Bachelor-und Masterstudiengang Physik vom 20.07.2011

Hiermit erkläre ich, Florian Wilhelm, dass ich die vorliegende Arbeit selbständig, ohne fremde Hilfe und ohne Benutzung anderer als der angegebenen Hilfsmittel angefertigt habe. Die aus fremden Quellen (einschließlich elektronischer Quellen) direkt oder indirekt übernommenen Gedanken sind ausnahmslos als solche kenntlich gemacht. Die Arbeit ist in gleicher oder ähnlicher Form oder auszugsweise im Rahmen einer anderen Prüfung noch nicht vorgelegt worden.

Frankfurt am Main, 29. September 2014